ARCHIVES
of
FOUNDRY ENGINEERING

10.24425/afe.2026.157970

Published quarterly as the organ of the Foundry Commission of the Polish Academy of Sciences

ISSN (2299-2944)
Volume 2026
Issue 1/2026

68 – 76

7/1

Automation of Porosity Morphology Evaluation in Castings

J. Majerník *, R. Bumbálek, T. Zoubek, P. Hanzal, K. Šramhauser, F. Špalek
University of South Bohemia in České Budějovice, Faculty of Agriculture and Technology, Czech Republic
* Corresponding author. E-mail address: jmajernik@fzt.jcu.cz

Received 30.07.25; accepted in revised form 22.10.25; available online 30.03.2026

Abstract

High pressure die casting technology is characterised by the production of high quality, complex shaped casts with good mechanical properties. However, die casts have a certain amount of porosity which can reduce their quality and mechanical properties. Mechanical properties are determined not only by the percentage of pores in the volume of the casting, but also by their geometric shape, taking into account the possibility of crack initiation at the edge of the pore. The shape and geometry of the pores are characterised by the roundness factor, which can be used to predict the mechanical properties of the castings. This paper addresses the problem of evaluating pore geometry with a view to automating the determination of the roundness factor and, at the same time, the percentage evaluation of the proportion of pores in the area of the metallographic section of the specimen. Metallographic sections are prepared from selected sets of casts, in which pore shape and quantity are automatically evaluated using selected image processing techniques. The roundness factor is defined, and the pores are classified into different categories based on this factor.

Keywords: Application of information technology to the foundry industry, Quality management, Metallography, Castings defects

1. Introduction

Among foundry technologies used in the casting of aluminum alloys for the automotive industry, the high-pressure die casting (HPDC) process holds a leading position. This predominance is mainly due to the minimal or even absent finishing operations required in the production of components [1]. Pressure-cast components are characterized by high dimensional accuracy, good mechanical properties, and low production costs. The good mechanical properties of casts are associated with their fine-grained structure, which forms due to the undercooling of the melt upon contact with the relatively cold mold cavity wall [2]. However, casts defects related to porosity and the presence of gases in the melt significantly affect the quality of the casts [3,4]. Porosity in casts mainly manifests as a reduction in mechanical properties and machinability. Air entrapment in the melt volume leads to reactions between oxygen and the melt's chemical components, resulting in oxide inclusions that may be distributed throughout the casting. In aluminum casts, the metal undergoes free-surface turbulence, where the initially oxidized skin comes into contact with the melt and other oxides, potentially forming double oxide films—bifilms—which eventually act as notches, reducing the casts' resistance to mechanical stress [5].

Due to the relatively high porosity of casts and the varying extent of air entrapment in cavities formed either by shrinkage or gas entrapment in the melt, identifying the type of porosity in HPDC casts is complex [4–7]. Generally, the presence of pores within casts is attributed to phase changes (liquid/solid). These cavities, ranging in size from microns to millimeters, depend on the type of metal alloy and the solidification process. The formation of cavities in cast structures is generally caused by melt shrinkage during solidification, gas distribution in the melt, or a combination of these factors, including gas porosity due to gas entrapment during the casting cycle [8–10].

Small cavities in aluminum alloy casts are commonly referred to as "bubbles" or "pores," with the resulting cast defect termed "bubbling," "porosity," or simply "pore formation." This is one of the most common defects in aluminum casts, primarily caused by changes in the solubility of hydrogen as the temperature of the aluminum alloy increases. In molten metal, hydrogen can be present only up to the limit defined by its solubility curve. As the metal cools, its hydrogen solubility decreases. When the equilibrium solubility limit is exceeded, hydrogen escapes from the melt either by diffusion or by forming gas bubbles—so-called endogenous bubbles, which are typically microscopic. Preventing the formation of such bubbles in gas-saturated metal during casting is practically impossible. The only effective strategy is prevention—avoiding hydrogen saturation of the molten metal in the first place. Endogenous bubbles form within the solidifying metal. They can arise through homogeneous or heterogeneous nucleation. Homogeneous nucleation involves the formation of nuclei directly from atomic clusters in the melt. In heterogeneous nucleation, nuclei form on foreign particles (e.g., oxides or chemical compounds) [11–13].

The nucleation mechanism of gas bubbles is influenced by the pressure conditions at the point of formation. Practically speaking, during crystallization, the solid phase encloses a microvolume of melt that cannot be refilled by liquid metal. This results in a vacuum, making microshrinkage zones ideal sites for hydrogen diffusion [14].

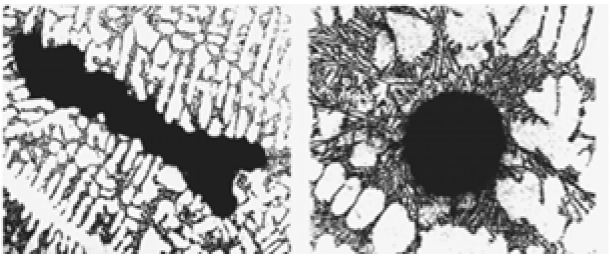

a) microshrinkage b) gas pore

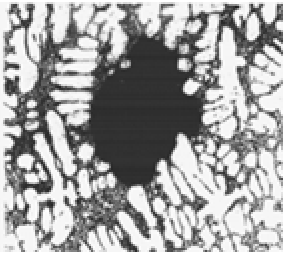

c) combination of gas pore and microshrinkahe

Fig. 1. The characteristic shape of the porosity [12]

Porosity is usually caused by a combination of bubbles and microshrinkage. It is rare to observe purely bubble-related or purely microshrinkage-related cavities. When bubble formation is dominant, the cavity tends to be spherical in shape (Figure 1b). When microshrinkage dominates, the resulting cavities are more complex and tend to mimic the dendritic structure of the metal (Figure 1a). The most common scenario is shown in Figure 1c, where the cavity is formed by a combination of a bubble and microshrinkage [12,13].

Exogenous bubbles form during casting when gases are present in the mold and gating system. They occur when the gas pressure in the mold or gating system exceeds the resistance imposed by the solidifying surface layer of the cast. The gases then penetrate the cast, forming characteristic spherical structures. Air bubbles can also form when the stream of molten metal falling from the ladle into the pouring basin entrains air, or when the metal swirls due to uneven filling of the gating system and mold, trapping air within the walls of the cast [15,16].

A key indicator of cast homogeneity is not only the percentage volume of pores or bubbles but also their geometric shape, particularly in terms of crack initiation risk at the pore edge. If gases are released in the form of round shapes, their impact on mechanical properties may be less severe compared to needle-like, planar, or plate-like pores. To evaluate cavities in the casting structure, a shape factor (f) is often introduced [12,13].

$$f = \frac{4.\pi.A_p}{U^2} \leq 1 \tag{1}$$

To determine the quantitative geometric parameters of the structure, the reciprocal value of the roundness factor s is also used:

$$s = \frac{U^2}{4.\pi.A_p} \geq 1 \tag{2}$$

For a spherical pore, the roundness factor value equals one. As the complexity and irregularity of the shape increase, so does the value of s (see Figure 2). This factor sensitively reflects the changing geometry of internal pores, which naturally affects the mechanical properties. Pores with a roundness factor s > 1 cause more disruption to the metal matrix, even at the same porosity percentage, than pores with s = 1. As the s factor increases, the notch effect of the pores increases, promoting crack formation in the structure, which in turn reduces the material's strength [12,13].

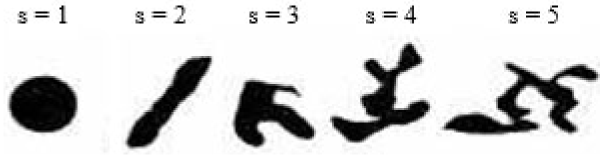

Fig. 2. Shapes of pores with different roundness factors „s“ [12]

In previous works [17–19] devoted to the influence of structural modifications of the gating system on the qualitative properties of casts, it was found that at different porosity values of the examined casts, certain samples showed very close values of mechanical properties. To explain this anomaly in the relationship between the mechanical properties of casts and porosity, as mentioned above, it is necessary to focus not only on the percentage content of porosity in metallographic sections in selected places of the casts (this partially expresses the pore size), but also on the shape of the pores. For this reason, the investigated and evaluated parameter is the roundness factor.

The presented article is devoted to the possibility of automating the evaluation of the morphology of pores in castings using innovative machine vision methods. The priority goal is to determine the possibility of introducing automation of pore evaluation with regard to the assessment of the correspondence of the detection of the shape and position of pores between expert determination by human factors and selected machine vision methods using image processing. The results presented in this article demonstrate that the introduction of image processing can significantly contribute to shortening the evaluation and detection of pores while maintaining the discrimination ability of the expert operator.

2. Experimental procedure

The shape, frequency of pores in the metallographic section, and the roundness factor of the pores were examined and evaluated on motor flange casts (Figure 3), produced using the high-pressure die casting method on a Müller Weingarten 600 cold-chamber horizontal die casting machine with a four-cavity mold. The characteristic properties of the cast are presented in Table 1.

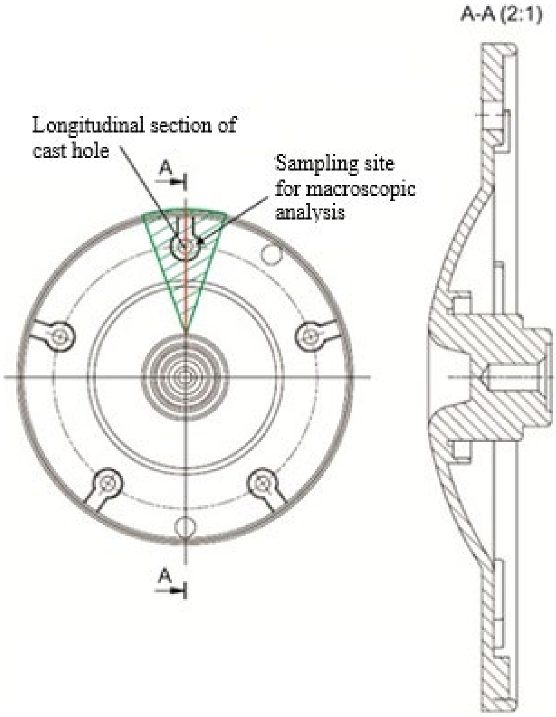

Fig. 3. Experimental sample

Table 1.
Weight and volume characteristics of the cast

Quantity	Value
Alloy	EN AC 47 100–AlSi12Cu1(Fe)
Alloy density, [kg.m^{-3}]	2650
Cast volume, [m^3]	51697.9 * 10^{-9}
Cast weight, [kg]	0.136
Cast diameter, [m]	0.1165
Characteristic wall thickness, [m]	0.002

Samples for the macroscopic study of pore shape, frequency, and roundness factor were taken from two locations within the gating system: from the structural opening area of the cast, as shown in Figure 3, and from the region of the main runner channel, as shown in Figure 4. The process and technological parameters of the casting cycle are listed in Table 2.

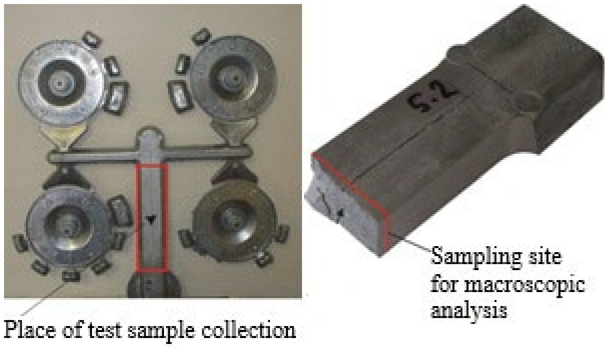

Fig. 4. Sampling scheme for macroscopic analysis

Table 2.
Technological parameters of the casting cycle

Parameter	Value
Melt temperature in filling chamber, °C	617
Die temperature, °C	200
Temperature of the tempering medium, °C	190
Final plunger velocity in 1st phase, m.s^{-1}	0.8
Plunger velocity in 2nd phase, m.s^{-1}	2.8
Holding pressure, MPa	25
Die cavity filling time, s	0.017

2.1. Description of Used Methods

The captured images of the samples were processed using selected thresholding methods. First, the images were converted from RGB to greyscale, and then pixel values were clipped to the range of 0 to 130, with this threshold value determined experimentally. Subsequently, based on thresholding algorithms, the image was converted to binary format, where pixels representing pores were assigned a value of 255 and the background a value of 0. The boundary curve points of the detected pores were then obtained, and the pixel area, relative area to the image, and roundness factor were calculated using formula (2).

The Otsu method is an automatic image thresholding technique used to convert grayscale images into binary images. Its goal is to find the threshold value that best separates the image into two classes, typically the object and the background [20]. The method is based on the image histogram, which is a set of bins representing the number of pixels at each brightness level, and is used to compute the threshold. The method assumes a bimodal histogram—i.e., that pixel intensities form two main groups [21]. The core idea of Otsu's method is to set the threshold between classes so that each class is as "homogeneous" as possible [22]. Key advantages of this method include its computational simplicity and its independence from the brightness and contrast of the original image [23]. The main computation in the Otsu method is represented by equation (4):

$$\sigma_b^2(t) = \omega_0(t)\,\omega_1(t)\,[\mu_0(t) - \mu_1(t)]^2 \tag{4}$$

where t is the tested threshold, $\omega_0(t)$ is the weight of class 0 with intensity ≤ t, $\omega_1(t)$ is the weight of class 1 with intensity > t, $\mu_0(t)$ is the mean intensity of class 0, $\mu_1(t)$ is the mean intensity of class 1, and $\sigma\_b^2(t)$ is the between-class variance [22].

The Multiple Otsu method is an extension of the standard Otsu method used for automatic image thresholding. While the basic Otsu method divides the image into two classes (e.g., object and background) [24], Multiple Otsu allows the image to be divided into more classes based on pixel intensity. The method searches for threshold values that divide the histogram into several regions in such a way that the between-class variance is maximized—i.e., the classes are as distinct as possible [25]. This is achieved by statistical analysis of the image histograms [26]. The total between-class variance in the Multiple Otsu method is calculated using equation (5):

$$\sigma_b^2 = \sum_{i=0}^{n-1} \omega_i (\mu_i - \mu_T)^2 \tag{5}$$

where n is the number of classes, ω_i is the probability of the i-th class, μ_i is the mean intensity of the i-th class, μ_T is the overall mean intensity of the image, and σ_b^2 is the total between-class variance [27].

The Yen method is an automatic image thresholding technique based on maximizing the entropy between two pixel classes—that is, between regions below and above a given threshold. The Yen method uses an information-theoretic approach to find the threshold that best separates these regions in terms of their internal entropy [28]. This often leads to better results in low-contrast or ambiguous histograms. It is particularly suitable for segmenting complex or noisy images [29]. In this method, the total correlation value $\{C_b(t) + C_f(t)\}$ is determined by probability distributions as described by equations (6–8).

$$C_b(t) = -ln\left\{\sum_{i=0}^{T}\left(\frac{p_i}{P_T}\right)^2\right\} \tag{6}$$

$$C_f(t) = -ln\left\{\sum_{i=T+1}^{255}\left(\frac{p_i}{1-P_T}\right)^2\right\} \tag{7}$$

$$t^* = argmax\{C_b(t) + C_f(t)\} \tag{8}$$

where p_i is the probability of occurrence of intensity i in the histogram and $P_T = \sum_{i=0}^{T-1} p_i$[27].

The Niblack method is a local thresholding technique that determines an individual threshold for each pixel based on the intensities in its surrounding neighborhood. For each small window around a given point, the mean and standard deviation are calculated [30-31]. The threshold in the Niblack method is determined using equation (9):

$$T(i,j) = \mu_{i,j} + k \cdot \sigma_{i,j} \tag{9}$$

where μ is the local mean, σ is the standard deviation, and k is a pre-defined constant, usually negative [32]. This approach adapts to local changes in brightness and contrast, making it suitable for text, document segmentation, and images with uneven lighting [33].

The Sauvola method is an adaptive thresholding technique derived from the Niblack method. It calculates the threshold for each pixel based on the local mean and standard deviation in its neighborhood [31]. Compared to the Niblack method, it also considers the maximum possible contrast in the image. This modification reduces noise in low-contrast areas, and the adjustable parameters can be fine-tuned for each case study [32]. The threshold value is calculated using equation (10):

$$T_{x,y} = \mu_{x,y}\left[1 - k\left(\frac{\sigma_{x,y}}{R} - 1\right)\right] \tag{10}$$

where μ is the local mean, σ is the standard deviation, R is the maximum contrast (usually 128 for 8-bit images), and k is a tunable parameter determining the sensitivity of the thresholding [33].

The Triangle method is a global thresholding technique that finds the optimal threshold based on the shape of the histogram by calculating the threshold that minimizes the variance of pixel intensities in the foreground and background. It connects two endpoints of the intensity histogram [34-36] and then finds the intensity level with the greatest perpendicular distance from this line. This intensity is then used as the threshold [37]. It is particularly suitable for images with a single dominant object and well-separated background. Equation (11) is used to calculate the perpendicular distance of a histogram point (x, y) from the line connecting points A = (x_0, y_0) and B = (x_1, y_1).

$$D(x,y) = \frac{|(y_1-y_0)x-(x_0-x_1)x+x_1y_0-y_1x_0|}{\sqrt{(y_1-y_0)^2+(x_1+x_0)^2}} \tag{11}$$

In equation (11), the value of x is sought for which this distance D (x, y) is maximal; this intensity is then selected as the threshold [38].

3. Results and Discussion

The capability of selected automatic image processing methods for pore detection on images of metal castings was tested on eight selected images. The same ten images were also manually evaluated by three experts in mechanical engineering technologies with experience in metal casting. Correlation analyses were performed on the obtained results for the detection of the total number of pores, analysis of the total pore area, and analysis of the average roundness of the detected pores. Additionally, an analysis of the time demands for processing the test images was conducted.

3.1. Correlation Analysis of Total Pore Count Detection

The aim of this analysis was to assess the level of agreement between evaluations of the total number of pores on selected metal cast images by three experts and six selected object segmentation methods in image data (Otsu, Multi-Otsu, Triangle, Yen, Niblack, and Sauvola). The results are presented in the form of a correlation matrix shown in Figure 5, which illustrates the mutual relationships between the individual evaluators and methods.

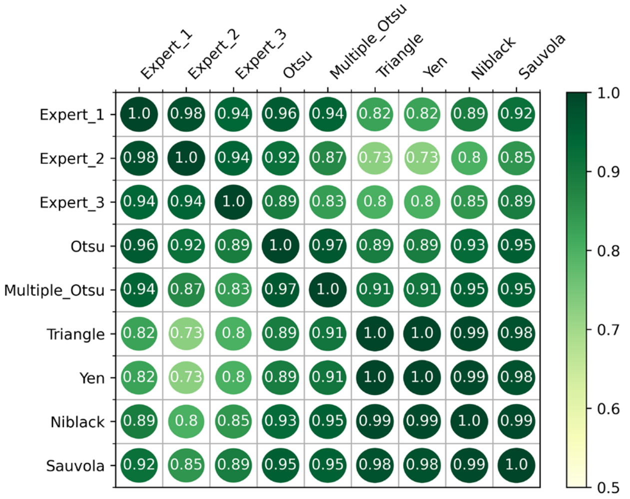

	Expert_1	Expert_2	Expert_3	Otsu	Multiple_Otsu	Triangle	Yen	Niblack	Sauvola
Expert_1	1.0	0.98	0.94	0.96	0.94	0.82	0.82	0.89	0.92
Expert_2	0.98	1.0	0.94	0.92	0.87	0.73	0.73	0.8	0.85
Expert_3	0.94	0.94	1.0	0.89	0.83	0.8	0.8	0.85	0.89
Otsu	0.96	0.92	0.89	1.0	0.97	0.89	0.89	0.93	0.95
Multiple_Otsu	0.94	0.87	0.83	0.97	1.0	0.91	0.91	0.95	0.95
Triangle	0.82	0.73	0.8	0.89	0.91	1.0	1.0	0.99	0.98
Yen	0.82	0.73	0.8	0.89	0.91	1.0	1.0	0.99	0.98
Niblack	0.89	0.8	0.85	0.93	0.95	0.99	0.99	1.0	0.99
Sauvola	0.92	0.85	0.89	0.95	0.95	0.98	0.98	0.99	1.0

Fig. 5. Correlation matrices of individual methods for determining the total number of pores on selected metallographic sections

The expert evaluations (Expert_1, Expert_2, Expert_3) show a very high degree of mutual correlation, with their correlation coefficients ranging from 0.94 to 0.98. This indicates strong consistency and agreement among the experts in evaluating the outputs. When comparing expert evaluations with automatic methods, the highest correlation values are achieved by the Otsu, Multiple Otsu, Niblack, and Sauvola methods, with correlations ranging from 0.85 to 0.96. These methods thus exhibit a high level of agreement with human evaluation and can be considered the most suitable to replace expert assessment in terms of identifying the total number of material defects in the given images, with the Otsu method achieving the best results among them. Conversely, the Triangle and Yen methods show lower correlations with the experts (particularly with Expert_2, only around 0.73), which may suggest a different segmentation approach or an inability to find the optimal threshold in these specific images. Very strong correlations are also observed among the automatic methods themselves, especially among Triangle, Yen, Niblack, and Sauvola, which show correlations between 0.98 and 1.0, indicating that their outputs are very similar. These methods are likely redundant in terms of their results.

3.2. Correlation Analysis of the Total Area of Detected Pores

This analysis focuses on evaluating the agreement between the three experts and six automatic thresholding methods based on determining the total area of pores captured in the selected metal cast images. The correlation matrix (Figure 6) generally shows very high correlation values, indicating that both expert evaluations and most methods provide consistent outputs.

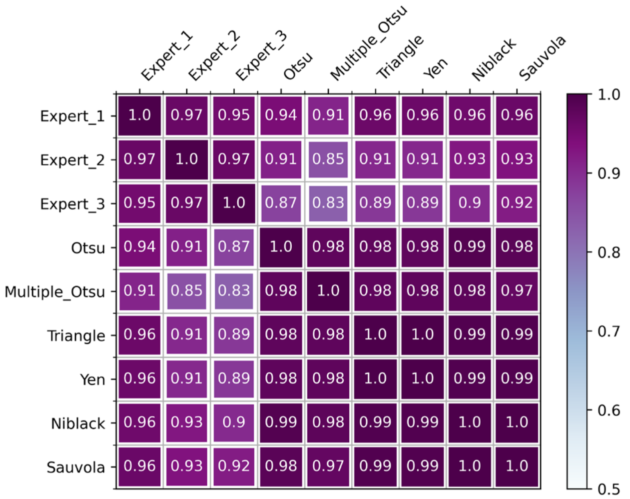

	Expert_1	Expert_2	Expert_3	Otsu	Multiple_Otsu	Triangle	Yen	Niblack	Sauvola
Expert_1	1.0	0.97	0.95	0.94	0.91	0.96	0.96	0.96	0.96
Expert_2	0.97	1.0	0.97	0.91	0.85	0.91	0.91	0.93	0.93
Expert_3	0.95	0.97	1.0	0.87	0.83	0.89	0.89	0.9	0.92
Otsu	0.94	0.91	0.87	1.0	0.98	0.98	0.98	0.99	0.98
Multiple_Otsu	0.91	0.85	0.83	0.98	1.0	0.98	0.98	0.98	0.97
Triangle	0.96	0.91	0.89	0.98	0.98	1.0	1.0	0.99	0.99
Yen	0.96	0.91	0.89	0.98	0.98	1.0	1.0	0.99	0.99
Niblack	0.96	0.93	0.9	0.99	0.98	0.99	0.99	1.0	1.0
Sauvola	0.96	0.93	0.92	0.98	0.97	0.99	0.99	1.0	1.0

Fig. 6. Correlation matrices for evaluating the total pore area on selected metallographic sections

Among the experts, a very high level of mutual agreement is evident. Correlation coefficients between them range from 0.95 to 0.97, confirming the consistency of human evaluation across different assessors and supporting the high validity of the experts' assessments. In terms of agreement with the experts, the best-performing methods are Niblack, Sauvola, Triangle, and Yen, which achieve correlations with individual experts in the range of 0.89 to 0.96. These methods show a very high degree of alignment with human evaluation and can be considered reliable alternatives to manual assessment. On the other hand, the Multiple Otsu method shows lower correlation values compared to the others, particularly with the third expert, where it only achieves a value of 0.83. The Otsu method also has slightly weaker correlations with the experts than the other methods mentioned, although it still remains at a relatively high level (around 0.87–0.94). Very strong correlations are also evident among the automatic methods themselves. Especially the Triangle, Yen, Niblack, and Sauvola methods are nearly perfectly correlated (with correlations of 0.99 to 1.0), indicating that their outputs are almost identical. Such a level of similarity can be leveraged in optimization, for example, by selecting a single representative method to simplify the model or reduce computational load.

3.3. Correlation Analysis of the Average Roundness of Detected Pores

This correlation analysis focuses on the relationships between the three expert assessments and the six binarization methods based on the evaluation of the average roundness of the pores detected by the respective experts or methods. This time, the correlation coefficients show higher variability and, in some cases, significantly lower values, including even negative correlations (see Figure 7).

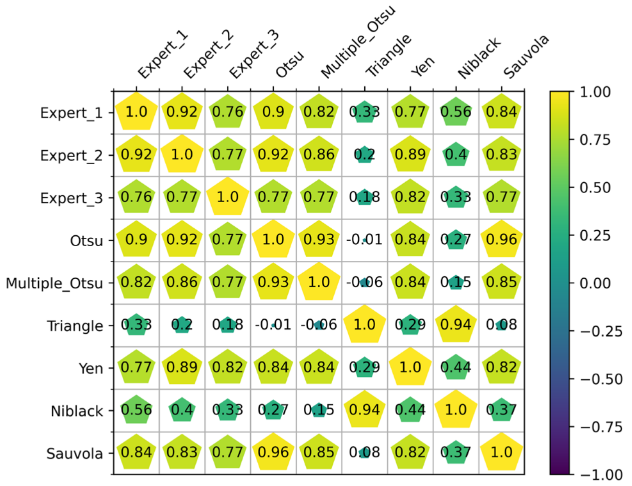

Fig. 7. Correlation matrices for evaluating the average roundness index of detected pores on selected metallographic sections

Among the individual experts, relatively strong agreement remains, though not as pronounced as in previous matrices. The correlations between them range from 0.76 to 0.92, suggesting some degree of variability in evaluation, particularly with Expert 3, who shows somewhat weaker correlation with the others. Among the methods, the highest correlations with the experts are shown by the Otsu method, which has very high agreement with all experts (0.90–0.92), as well as the Sauvola and Yen methods, which also consistently achieve high correlations (0.77–0.85). The Multiple Otsu method maintains strong correlation with both the experts and the Otsu method (0.82–0.93). In contrast, the Triangle method shows the lowest correlations with nearly all experts (values around 0.18–0.33) and even negative or zero correlation with other methods (e.g., with Otsu or Multiple Otsu). This indicates that the outputs of the Triangle method differ significantly from both human assessments and other algorithms, suggesting its unsuitability for this particular task. The Niblack method also has relatively low correlations with the experts (0.33–0.56) and weak or even negative relationships with some of the other methods, which also questions its consistency for this task.

Overall, the results show that while the Otsu, Sauvola, Yen, and Multiple Otsu methods demonstrate consistent agreement with the experts and among themselves, the Triangle method and, to a lesser extent, Niblack differ and may produce outputs that do not align with human evaluation based on this specific metric.

3.3. Time Analysis of Image Processing by Individual Methods

During the processing of individual images—which involved detecting pores in cast—the time required by each expert and each automatic thresholding method to complete the task was recorded. All these times are presented in Table 3.

The difference between manual evaluation by experts and automatic evaluation using conventional image processing algorithms is substantial. The average evaluation time for experts was 2,352.62 seconds, whereas the average time for processing the images using automatic methods was 0.28 seconds, which is 8,272 times less. The Otsu method was the fastest at processing the selected representative images, mainly due to a significant time saving on the first image, where it outperformed all other methods by at least 0.21 seconds—which, given its processing time of 0.014 seconds, means it was at least 18 times faster. If the first image were excluded, it would rank as the third fastest method after Yen and Triangle.

Table 3.
Time required (s) for processing individual test images of metallographic sections containing porosity

	Expert1	**Expert2**	**Expert3**	**Otsu**	**Multiple Otsu**	**Triangle**	**Yen**	**Niblack**	**Sauvola**
img_1	255	322	183	0,014	0,247	0,224	0,226	0,246	0,227
img_2	239	273	153	0,010	0,016	0,006	0,006	0,014	0,015
img_3	360	354	205	0,011	0,018	0,008	0,007	0,015	0,016
img_4	107	69	41	0,009	0,010	0,006	0,007	0,014	0,015
img_5	801	993	357	0,012	0,017	0,010	0,009	0,018	0,018
img_6	576	354	183	0,010	0,020	0,010	0,010	0,018	0,015
img_7	287	384	175	0,010	0,019	0,007	0,007	0,018	0,015
img_8	48	146	96	0,010	0,021	0,008	0,007	0,015	0,015
sum	2771	2894	1393	0,09	0,37	0,28	0,28	0,36	0,34

3.4. Application Example of Selected Thresholding Methods on Test Images

Selected images comparing the detection performance of the automatic methods Otsu, Yen, and Sauvola, and three experts are shown in Figures 8 and 9. In Figure 8, there is optimal agreement among both the experts and the presented methods regarding the location and shape of the individual detected pores, which forms the basis for determining their roundness in the metal casting. In Figure 9, there is a high correlation in detecting the individual pores, although the automatic methods tend to detect even small features that the experts did not mark, as they did not consider them to be pores but rather image noise. Additionally, a slight mismatch in the exact shape—and thus the related roundness—of some pores can be observed between the selected methods and the individual experts. For example, in Figure 8, Expert 1 and Expert 3 assessed two pores with roundness values of 3 and 4 as absent, whereas Expert 2 identified three pores with a roundness of 4 and one with a roundness of 3 in the image.

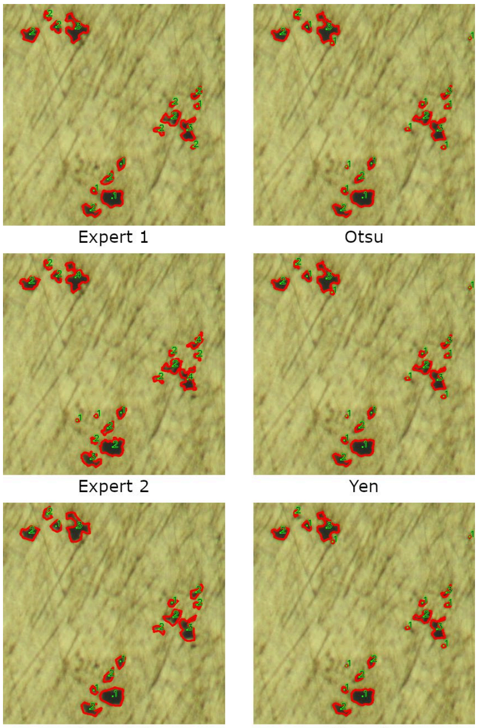
Expert 1 Otsu
Expert 2 Yen
Expert 3 Sauvola

Fig. 8. Example of processing a test image by three experts and selected automatic methods

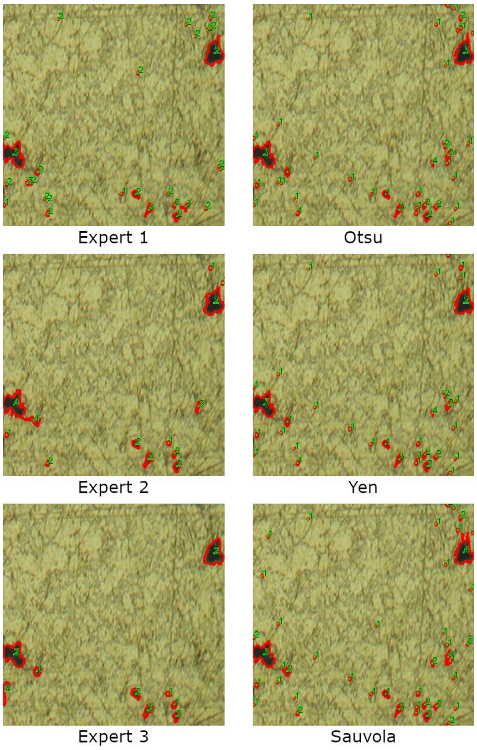
Expert 1 Otsu
Expert 2 Yen
Expert 3 Sauvola

Fig. 9. Example of processing a test image by three experts and selected automatic methods

4. Conclusions

Three correlation analyses were conducted to assess the level of agreement between the evaluations of three experts and six automatic image binarization methods. Each analysis used a different type of metric: the total number of detected pores, the total area of detected pores, and the average roundness of the detected pores. The results highlight differences in consistency among the individual methods depending on the selected metric.

In the analysis focused on the agreement in the number of detected pores, the results show very strong correlations between the individual experts (0.94–0.98), confirming the consistency of human evaluation. Among the automatic methods, the highest agreement with the experts was found in the Otsu, Multiple Otsu, Niblack, and Sauvola methods, with correlation values around 0.89–0.96. In contrast, the Triangle and Yen methods had lower correlations (0.73–0.82), indicating discrepancies between their outputs and expert judgment.

The second analysis was based on the correlation of the total area of detected pores. Here again, the correlations were very high—both among the experts (0.95–0.97) and between the experts and methods such as Niblack, Sauvola, Triangle, and Yen (around 0.89–0.96). In this metric, the Triangle method, which showed weaker performance in the previous matrix, appears to be fully relevant and aligned with human evaluation. A significant correlation (0.98–1.0) among the Triangle, Yen, Niblack, and Sauvola methods indicates a high similarity in their outputs.

These methods could be considered interchangeable, which may be useful for reducing redundant computations.

In the third correlation analysis, the results were lower and more variable. While a valid degree of agreement remained among the experts (0.76–0.92), the outputs of some methods differed significantly. The Otsu, Multiple Otsu, Sauvola, and Yen methods maintained high correlation with the experts (0.77–0.96), thus demonstrating strong consistency. Conversely, the Triangle method showed very low, sometimes even negative correlations (e.g., −0.01 with Otsu), indicating that its output is completely inconsistent with other approaches for this task. The Niblack method also showed lower correlations, confirming its lower reliability in relation to this specific metric.

In terms of time savings, all automatic methods significantly outperformed manual annotation of individual pores in the images of metal castings. All automatic methods were able to process the test images in under 0.5 seconds, whereas the experts took approximately 26–55 minutes for the same task.

Based on the obtained results, it can be concluded that for processing images of the same type as those used in this study—specifically for the detection of pores in cast—the Otsu, Sauvola, Yen, and Multiple Otsu methods are particularly suitable due to their consistency and correlation with expert manual detection across all three analyses. Their main advantage lies in the significant time savings and the potential to allocate expert effort to more sophisticated tasks. The remaining methods, Triangle and Niblack, did not demonstrate sufficient relevance for this type of task. The Triangle method failed in determining the average roundness of detected pores, where the Niblack method also showed weaker results.

The conclusions reached will serve as a platform for further research and at the same time predict the possibilities of introducing automatic image processing methods into casts quality assurance systems. These methods should be included in the technical preparation of production when developing new pressure casting die when sampling the first zero-series casts. At the same time, ongoing research aims to find a correlation between the shape of pores and the mechanical properties of casts. This will allow automatic porosity assessment methods to be used in the output control of casts, where, referring to the partial conclusions of publications [17–19], it is possible to predict the state that even with a higher porosity fraction with a circularity index approaching the value s = 1, it is possible to maintain the required values of mechanical properties and either release the casts for production or ship them directly.

References

[1] Cao, H., Luo, Z., Wang, C., Wang, J., Hu, T., Xiao, L. & Che, J. (2020). The stress concentration mechanism of pores affecting the tensile properties in vacuum die casting metals. *Materials.* 13(13), 1-14. DOI: 10.3390/ma13133019.

[2] Dou, K., Lordan, E., Zhang, Y.J., Jacot, A. & Fan, Z.Y. (2019). Numerical simulation of fluid flow, solidification and defects in high pressure die casting (HPDC) process. *IOP Conference Series: Materials Science and Engineering.* 529(1), pp. 1-6. DOI: 10.1088/1757-899X/529/1/012058.

[3] Zhao, X., Wang, P., Li, T., Zhang, B.-Y., Wang, P., Wang, G.-Z. & Lu, S.-Q. (2018). Gating system optimization of high pressure die casting thin-wall AlSi10MnMg longitudinal loadbearing beam based on numerical simulation. *China Foundry.* 15(6), 436-442. DOI: 10.1007/s41230-018-8052-z.

[4] Dybalska, A., Caden, A., Griffiths, W. D., Nashwan, Z., Bojarevics, V., Djambazov, G., Tonry, C.E.H. & Pericleous, K. A. (2021). Enhancement of mechanical properties of pure aluminium through contactless melt sonicating treatment. *Materials*. 14(16), 4479, 1-16. DOI: 10.3390/ma14164479.

[5] Otsuka, Y. (2014). Experimental verification and accuracy improvement of gas entrapment and shrinkage porosity simulation in high pressure die casting process. *Materials Transactions*. 55(1), 154-160. DOI: 10.2320/matertrans.F-M2013835.

[6] Majidi, S.H. & Beckermann, C. (2019). Effect of pouring conditions and gating system design on air entrainment during mold filling. *International Journal of Metalcasting*. 13(2), 255-272. DOI: 10.1007/s40962-018-0272-x.

[7] Gaspar, S., Majernik, J. & Kolinsky, J. (2021). Analysis of causes of porosity change of castings under the influence of variable biscuit height in the filling chamber. *Materials*. 14(22), 6827, 1-12. DOI: 10.3390/ma14226827.

[8] Ignaszak, Z. & Hajkowski, J. (2015). Contribution to the identification of porosity type in AlSiCu high-pressure-die-castings by experimental and virtual way. *Archives of Foundry Engineering.* 15(1), 143-151. DOI: 10.1515/afe-2015-0026.

[9] Cao. H. & Wessén, M. (2004). Effect of microstructure on mechanical properties of as-cast Mg-Al alloys. *Metallurgical & Materials Transactions A*. 35(1), 309-319. DOI: 10.1007/s11661-004-0132-6.

[10] Otarawanna. S., Gourlay, C.M., Laukli, H.I. & Dahle, A.K. (2009). Microstructure formation in AlSi4MgMn and AlMg5Si2Mn high-pressure die castings. *Metallurgical and Materials Transactions A*. 40(7), 1645-1659. DOI: 10.1007/s11661-009-9841-1.

[11] Gašpár, Š., Paško, J., Majerník, J. (2017). *Influence of structure adjustment of gating system of casting mould upon the quality of die cast.* Lüdenscheid: RAM-Verlag.

[12] Paško, J., Gašpár, Š. (2014). *Technological Factors of Die Casting.* Lüdenscheid: RAM-Verlag.

[13] Ružbarský, J., Paško, J., Gašpár, Š. (2014). *Techniques of Die casting*. Lüdenscheid: RAM-Verlag.

[14] Altuncu, E., Doğan, A. & Ekmen, N. (2019). Performance evaluation of different air venting methods on high pressure aluminum die casting proces. *Acta Physica Polonica A*. 135(4), 664-667. DOI: 10.12693/APhysPolA.135.664.

[15] Qin, X.-Y., Su, Y., Chen, J. & Liu, L.-J. (2019). Finite element analysis for die casting parameters in high-pressure die casting proces. *China Foundry*. 16(4), 272-276. DOI: 10.1007/s41230-019-8088-8.

[16] Cleary, P.W., Savage, G., Ha, J. & Prakash, M. (2014). Flow analysis and validation of numerical modelling for a thin walled high pressure die casting using SPH. *Computational Particle Mechanics*. 1(3), 229-243. DOI: 10.1007/s40571-014-0025-4.

[17] Majernik, J. & Gaspar, S. (2019). Analysis of interaction between position of gate and selected properties of low-weight casts on the silumin basis. *Archives of Foundry Engineering*. 19(3), 106-110. DOI: 10.24425/afe.2019.129619.

[18] Majernik, J., Gaspar, S., Kmec, J., Karkova, M. & Mascenik, J. (2020). Possibility of utilization of gate geometry to modify the mechanical and structural properties of castings on the Al-Si Basis. *Materials*. 13(16), 3539, 1-15. DOI: 10.3390/MA13163539.

[19] Gaspar, S., Coranic. T., Majernik, J., Husar, J., Knapcikova, L., Gojdan, D. & Pasko, J. (2021). Influence of gating system parameters of die-cast molds on properties of al-si castings. *Materials*. 14(13), 3755, 1-18. DOI: 10.3390/ma14133755.

[20] Otsu, N. (1979). A threshold selection method from gray-level histograms. *Automatica.* 11(285-296). DOI: 10.1109/TSMC.1979.4310076.

[21] Oliva, D., Abd Elaziz, M., & Hinojosa, S. (2019). Otsu's between class variance and the tree seed algorithm**.** In *Metaheuristic Algorithms for Image Segmentation: Theory and Applications* (pp. 71–83). Springer, Cham.

[22] Tulyakov, T.F. & Afanaseva, O.V. (2026). Comparative analysis of image segmentation methods in power line monitoring systems. *International Journal of Engineering*. 39(1), 1-11. DOI: 10.5829/ije.2026.39.01a.01.

[23] You, N., Han, L., Liu, Y., Zhu, D., Zuo, X. & Song, W. (2023). Research on wavelet transform modulus maxima and OTSU in edge detection. *Applied Sciences*. 13(7), 4454, 1-15. DOI: 10.3390/app13074454.

[24] Zhang, A, Han, Z., Sun, G., Chen, X., Cheng, J. & Zhang, H. (2025). An impervious surfaces extraction method based on optical, ascending and descending SAR remote sensing imagery in high-density urban core areas. *International Journal of Applied Earth Observation and Geoinformation*. 140, 104595, 1-15. DOI: 10.1016/j.jag.2025.104595.

[25] Huo, W., Li, R.Y.M. & Zhu, Z. (2025). Developing a program for quantification and characterization of microstructure: Application to BSE images of geopolymer recycled concrete. *Journal of Building Engineering*. 104, 112290, 1-12. DOI: 10.1016/j.jobe.2025.112290.

[26] López-Gómez, J.J., Estévez-Asensio, L., Cebriá, Á., Izaola-Jauregui, O., Pérez López, P., González-Gutiérrez, J., Primo-Martín, D., Jiménez-Sahagún, R., Gómez-Hoyos, E., Rico-Bargues, D., Godoy, E.J. & De Luis-Román, D.A. (2025). Artificial intelligence-assisted muscular ultrasonography for assessing inflammation and muscle mass in patients at risk of malnutrition. *Nutrients*. 17(10), 1620, 1-19. DOI: 10.3390/nu17101620.

[27] Serbet, F. & Kaya, T. (2025). New comparative approach to multi-level thresholding: chaotically initialized adaptive meta-heuristic optimization methods. *Neural Computing and Application.* 37(14), 8371-8396. DOI: 10.1007/s00521-025-11016-9.

[28] Yen, J.-Ch., Chang, F.-J. & Chang, S. (1995). A new criterion for automatic multilevel thresholding. *IEEE Transactions on Image Processing*. 4(3), 370-378. DOI: 10.1109/83.366472.

[29] Khan, A., Garner, R., La Rocca, M., Salehi, S. & Duncan, D. (2023). A novel threshold-based segmentation method for quantification of COVID-19 lung abnormalities. *Signal, Image and Video Processing.* 17(4), 907-914. DOI: 10.1007/s11760-022-02183-6.

[30] Springer Nature Link. (2020). Retrieved June 4, 2020, from https://doi.org/10.1007/s11831-020-09416-2.

[31] Niblack, W. (1985). *An Introduction to Digital Image Processing*. Strandberg Publishing Company.

[32] Zhang, M., Wang, J., Cao, X., Xu, X., Zhou, J. & Chen, H. (2024). An integrated global and local thresholding method for segmenting blood vessels in angiography. *Heliyon*. 10(22), e38579, 1-22. DOI: 10.1016/j.heliyon.2024.e38579.

[33] Hamadi, H., Ardi, H., Mulyono, T., Muhtadan. (2022). Segmentation of betatron SEA 7 radiographic images with computed radiography on steel specimen. In 8th International Conference on Science and Technology, 7-8 September 2022. DOI: 10.1109/ICST56971.2022.10136255.

[34] Sauvola J., Pietikäinen, M. (2000). Adaptive document image binarization. *Pattern Recognition*. 33(2), 225-236. DOI: 10.1016/S0031-3203(99)00055-2.

[35] Van L.N., Nguyen, G.V., Kim, Y., Do, M.T.T., Kwon, S., Lee, J. & Lee, G. (2025). Rapid urban flood detection using PlanetScope imagery and thresholding methods. *Water*. 17(7), 1005, 1-21. DOI: 10.3390/w17071005.

[36] Ghimire, A., Chung, Y.S., Jeong, S. & Kim, Y. (2025). Python algorithm package for automated Estimation of major legume root traits using two dimensional images. *Scientific Reports.* 15(1), 7341, 1-15. DOI: 10.1038/s41598-025-91993-y.

[37] Zack, G.W., Rogers, W.E. & Latt, S.A. (1977). Automatic measurement of sister chromatid exchange frequency. *Journal of Histochemistry & Cytochemistry*. 25(7), 741-753. DOI: 10.1177/25.7.70454.

[38] Haupts, P.J., Al-Joumma, H., Al-Shrouf, L. & Jelali, M. (2025). Comparative analysis of binarization approaches for automated dye penetrant testing. *Processes*. 13(4), 1212, 1-28. DOI: 10.3390/pr13041212.